Sub-type specific connectivity between CA3 pyramidal neurons may underlie their sequential activation during sharp waves

Rosanna P. Sammons[1,7]*, Stefano Masserini[2,3,4]*, Laura Moreno-Velasquez[1], Verjinia D. Metodieva[1,4], Gaspar Cano[2], Andrea Sannio[1], Marta Orlando[1,7], Nikolaus Maier[1], Richard Kempter[2,3,4], Dietmar Schmitz[1,3,4,5,6,7]

April 9, 2024

[1]Charité-Universitätsmedizin Berlin, corporate member of Freie Universität Berlin and Humboldt-Universität zu Berlin, Neuroscience Research Center, Berlin, 10117, Germany

[2]Institute for Theoretical Biology, Department of Biology, Humboldt-Universität zu Berlin, Berlin, 10115, Germany

[3]Bernstein Center for Computational Neuroscience Berlin, Berlin, 10115, Germany

[4]Charité-Universitätsmedizin Berlin, corporate member of Freie Universität Berlin and Humboldt-Universität zu Berlin, Einstein Center for Neurosciences Berlin, Berlin, 10117, Germany

[5]German Center for Neurodegenerative Diseases (DZNE) Berlin, Berlin, 10117, Germany

[6]Max-Delbrück Center for Molecular Medicine in the Helmholtz Association, Berlin, 13125, Germany

[7]Charité – Universitätsmedizin Berlin, corporate member of Freie Universität Berlin and Humboldt-Universität zu Berlin, NeuroCure Cluster of Excellence, 10117 Berlin, Germany

* These authors contributed equally to this work.

Abstract

The CA3 region of the hippocampus is the major site of sharp wave initiation, a form a network activity involved in learning and memory. Highly recurrent connectivity within its excitatory network is thought to underlie processes involved in memory formation. Recent work has indicated that distinct subpopulations of pyramidal neurons within this region may contribute differently to network activity, including sharp waves, in CA3. Exactly how these contributions may arise is not yet known. Here, we disentangle the local connectivity between two distinct CA3 cell types: thorny and athorny pyramidal cells. We find an asymmetry in the connectivity between these two populations, with athorny cells receiving strong input from both athorny and thorny cells. Conversely, the thorny cell population receives very little input from the athorny population. Computational modelling suggests that this connectivity scheme may determine the sequential activation of these cell types during large network events such as sharp waves.

Introduction

Diversity among pyramidal neuron populations is often overlooked when considering the role of these cells within neuronal circuits. Despite reports of variation within the pyramidal population in the hippocampus (Bilkey and Schwartzkroin, 1990; Fitch et al., 1989), much more attention has been paid to the heterogeneity of interneurons. However, several studies have reported functional and morphological heterogeneity within the pyramidal CA3 cell population (Bilkey and Schwartzkroin, 1990; Sun et al., 2017; Marissal et al., 2012; Lee et al., 2015). Attention is now turning to this rich assortment of pyramidal cells, and recent efforts have begun to tease apart the distinct roles of these sub-types in functional circuits (Cembrowski and Spruston, 2019; Soltesz and Losonczy, 2018; Valero and de la Prida, 2018). In the hippocampus, CA3 is considered the main generator of sharp waves (SPWs), and thus, plays an integral role in memory consolidation. A recent study described two distinct sub-types of CA3 pyramidal neurons, differentiated by the presence or absence of complex spine structures called thorny excrescences (the post-synaptic site of input coming from mossy fibres of the dentate gyrus granule cells) (Hunt et al., 2018). The study showed that cells lacking these thorny excrescences, termed athorny pyramids, fire before thorny pyramids during SPWs (Hunt et al., 2018). Therefore, it is proposed that athorny cells play an important role in SPW initiation and, in turn, in memory processing in CA3. However, it is unknown how these two sub-types of pyramidal neuron are embedded in the local microcircuit. We have previously shown that CA3 pyramidal cells connect to each other at a high rate (8.8 %) (Sammons et al., 2024). Here, we investigate the local sub-type specific connectivity between thorny and athorny CA3 pyramids and find a distinct asymmetry. When implementing this asymmetry into a computational model, we find that sub-type specific connectivity is crucial for the distinct firing times of athorny and thorny cells during SPWs.

Results & Discussion

To examine the connectivity between thorny and athorny pyramidal cells in CA3, we performed whole-cell patch clamp recordings from up to 8 cells simultaneously. Cells were posthoc classified as thorny or athorny using biocytin labelling and confocal microscopy to determine the presence or absence of thorny excrescences (Fig. 1A). In total, we recorded from 348 CA3 pyramids, of which 229 were thorny and 119 were athorny (Fig. 1B). We measured the distance from the soma to the first branch on the apical dendrite and found that thorny cells branched significantly closer to the soma than athorny cells (Fig. 1C; median [IQR] for thorny: 12.5 [20.9] μm, athorny: 51.4 [38.0] μm; $p < 0.001$, Mann-Whitney-U test). Furthermore, we found that athorny cells tended to be located deeper in the pyramidal layer, towards the stratum oriens. Meanwhile, thorny cells were found throughout the deep-superficial axis of the pyramidal cell layer (Fig. 1D, median [IQR] for thorny: 28 [32] μm, athorny: 12 [14] μm, $p < 0.001$, Mann-Whitney-U test). These results resemble findings from Marissal et al. (2012) who observed similar differences in soma location and primary apical dendritic length between early and late born CA3 neurons, suggesting that thorny and athorny neurons may be developmentally distinct.

Next, we looked at connection rates between these two pyramidal populations. In our whole-cell patch clamp recordings, each cell was stimulated to elicit 4 action potentials, and post-synaptic traces were

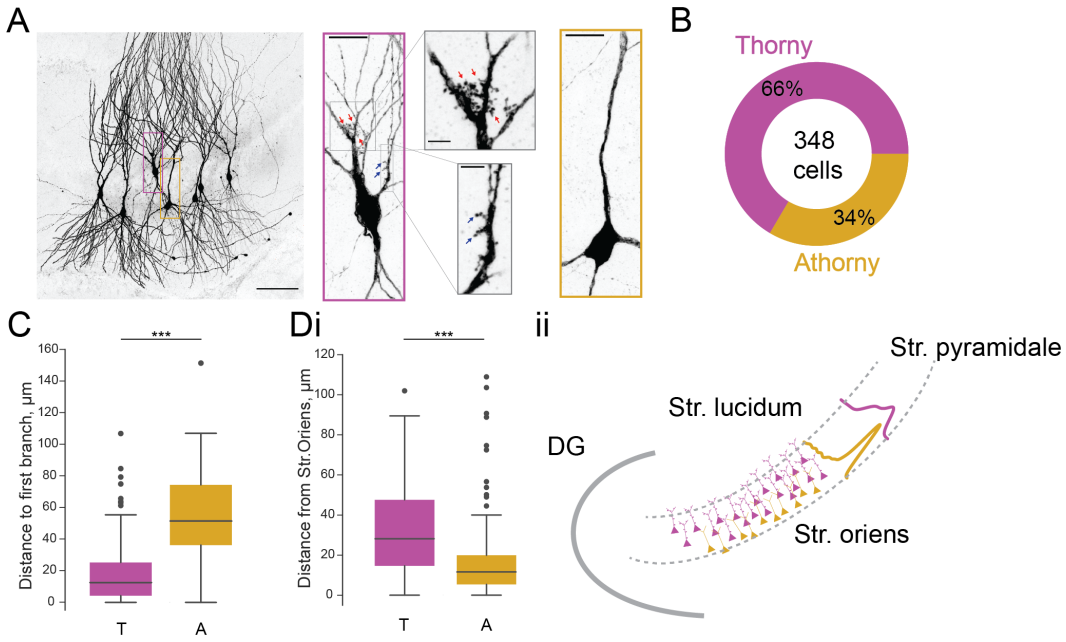

Figure 1: Proportion and distribution of thorny and athorny pyramidal neurons in CA3. A, Left, Image of 7 pyramidal neurons recorded simultaneously and filled with biocytin to reveal thorny and athorny morphologies. Right, magenta box contains a typical example of a thorny CA3 pyramid, grey boxes show close up of regions with thorns; yellow box shows a typical athorny pyramidal neuron. Scale bar in left image 100 μm, in magenta/yellow boxed insets 20 μm, in grey boxed insets 5 μm. **B**, Proportion of thorny and athorny cells in total recorded pyramidal neurons. **C**, Distance from soma to the first branch point for thorny (T) and athorny (A) CA3 pyramidal neurons. **Di**, Location of thorny and athorny cell somata across the deep-superficial axis of the pyramidal layer. **Dii**, Schematic depicting the distribution of thorny and athorny pyramids in the deep-superficial axis of the CA3 pyramidal layer.

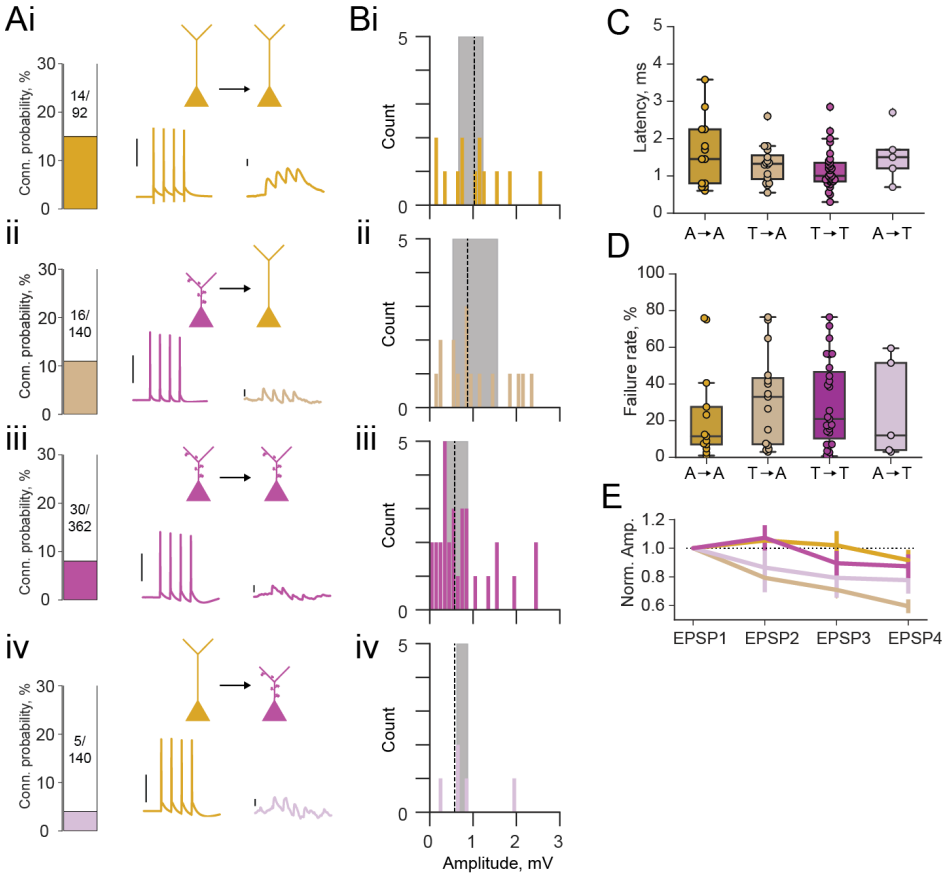

Figure 2: Properties of excitatory connections between athorny and thorny CA3 pyramids. **A**, Connection probabilities and example connections between: **i**, athorny cells, **ii**, thorny and athorny cells, **iii**, thorny cells and **iv**, athorny and thorny cells. Scalebars for presynaptic action potentials, 40 mV; for postsynaptic responses, 0.5 mV. **B**, Histograms of synaptic amplitudes of the different connection types: **i**, athorny-athorny, **ii**, thorny-athorny, **iii**, thorny-thorny, **iv**, athorny-thorny. Dashed line represents median value and shaded area interquartile range. **C**, Latency of synaptic connections onto postsynaptic athorny cells, individual points show single connection values. **D**, Failure rates of the different synaptic connection types. **E**, Short-term plasticity dynamics of different synaptic connection types. Synaptic amplitudes are normalised to the first EPSP in the train of 4.

examined for potential synaptic coupling. We found a high rate of connectivity (15%) between athorny cells (Fig. 2Ai), and from thorny onto athorny cells (11%; Fig. 2Aii). Thorny cells connected to each other at a rate of 8% (Fig. 2Aiii). Meanwhile, connections from athorny onto thorny cells were the least common, occurring at a rate of 4% (Fig. 2Aiv). The overall rate of connectivity (65/734 = 8.9 %) corresponds well to our previously reported high level of connectivity within the general CA3 pyramidal population (8.8 %) (Sammons et al., 2024). Synaptic connections were strongest amongst athorny-athorny cells, although no statistically significant differences were present across connection types (Fig. 2Bi, median [IQR] amplitudes

for athorny-athorny: 1.08 [0.56] mV; ii, thorny-athorny: 0.88 [1.03] mV; iii, thorny-thorny: 0.57 [0.55] mV; iv, athorny-thorny: 0.66 [0.25] mV; $p = 0.370$, Kruskal-Wallis test). EPSPs across all connection types had latencies below 3 ms (with the exception of a single connection between two athorny cells which had a latency of 3.58 ms) indicating that identified connections were monosynaptic (Fig. 2C). We further looked at the failure rate of each synapse type. Athorny-athorny synapses had the lowest failure rate, although no statistical difference was observed between groups (Fig. 2D, median [IQR] failure rate for athorny-athorny: 11.5 [20.5] %, thorny-athorny: 33.0 [36.2] %, thorny-thorny: 21.0 [36.3] %, athorny-thorny: 12.0 [47.5] %, p=0.729, Kruskal-Wallis test). Additionally, we looked at synaptic dynamics to determine if synapse types had different plasticity qualities. Connections from thorny onto athorny neurons showed significantly more synaptic depression than athorny-athorny connections (Fig. 2E; $p = 0.008$ Kruskal-Wallis followed by Dunn's posthoc with Bonferroni correction; all other comparisons $p > 0.05$).

To determine the overall impact of each connection type within the local network, we calculated the synaptic product. This metric takes into account connection probability (Fig. 3Ai), connection strength (Fig. 3Aii), and size of the presynaptic population (Fig. 3Aiii), thereby giving an estimate of how large the input onto the particular cell type is for any given presynaptic population. Thorny-athorny connections show the highest synaptic product, followed by athorny-athorny connections (Fig. 3Aiv). Together, our results demonstrate a strong pattern of input onto athorny neurons and much weaker input onto thorny cells, particularly from the athorny sub-population (Fig. 3B).

Athorny (A) cells have been reported to fire before thorny (T) cells during SPWs (Hunt et al., 2018) suggesting that activity flows along this axis. The low athorny-thorny (A→T) and the high thorny-athorny (T→A) connectivities might thus appear surprising. To understand what dynamics such a CA3 microcircuit implies, we constructed a model network in which T and A neurons are connected according to the experimentally observed connectivities (Fig. 4A). In addition to the two pyramidal cell populations, we included two classes of interneurons that have been suggested to play fundamental roles in SPW generation:

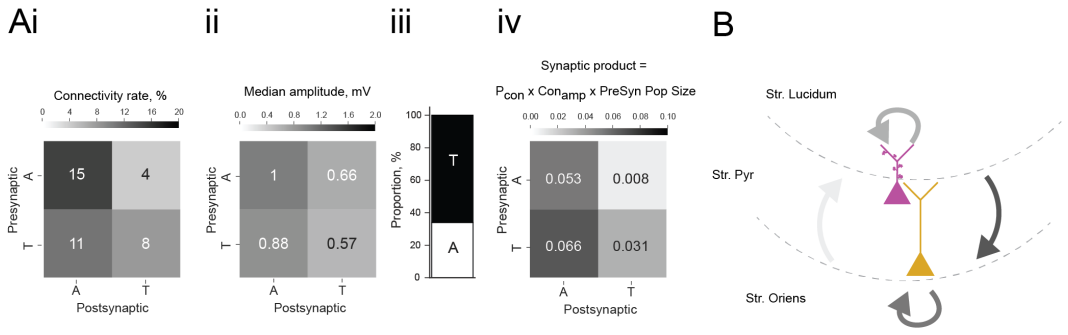

Figure 3: Summary of overall impact of each connection type. **Ai**, Matrix showing connection rates between the four combinations of connection types, **ii**, matrix showing mean connection strength for the four connection types, **iii**, proportion of each cell type found in the CA3 pyramidal population, **iv**, matrix showing the synaptic product, calculated as the product of the matrices in i and ii multiplied by the presynaptic population size shown in iii. **B**, Schematic depicting the connections between the two pyramidal cell types in the CA3, line colour is coded by connection impact.

PV$^+$ basket cells (B), which are active during SPWs, and a putative class of anti-SPW interneurons (C), which fire during non-SPW (NSPW) times and keep the other populations inhibited (Evangelista et al., 2020). Strong reciprocal coupling between the two inhibitory populations gives rise to an underlying SPW-NSPW bistability, and the network alternates between these two states due to adaptation in pyramidal cells, as proposed by Levenstein et al. (2019) as the driving mechanism of SPWs. We tuned model parameters (see Materials and Methods) such that the event incidence is ≈ 1/s (with stochastic onset timings driven by finite-size fluctuations) and the average event duration is ≈ 80 ms.

An event starts when B cells suppress enough C cells to disinhibit pyramidal neurons, which increase activity if their adaptive currents are weak enough. Athorny neurons activate first, due to their lower rheobase (documented by Hunt et al. (2018), Linaro et al. (2022), and our own data (Fig. S1)) and steeper f-I curve (Hunt et al., 2018; Linaro et al., 2022). Thorny neurons follow them in a clearly distinct

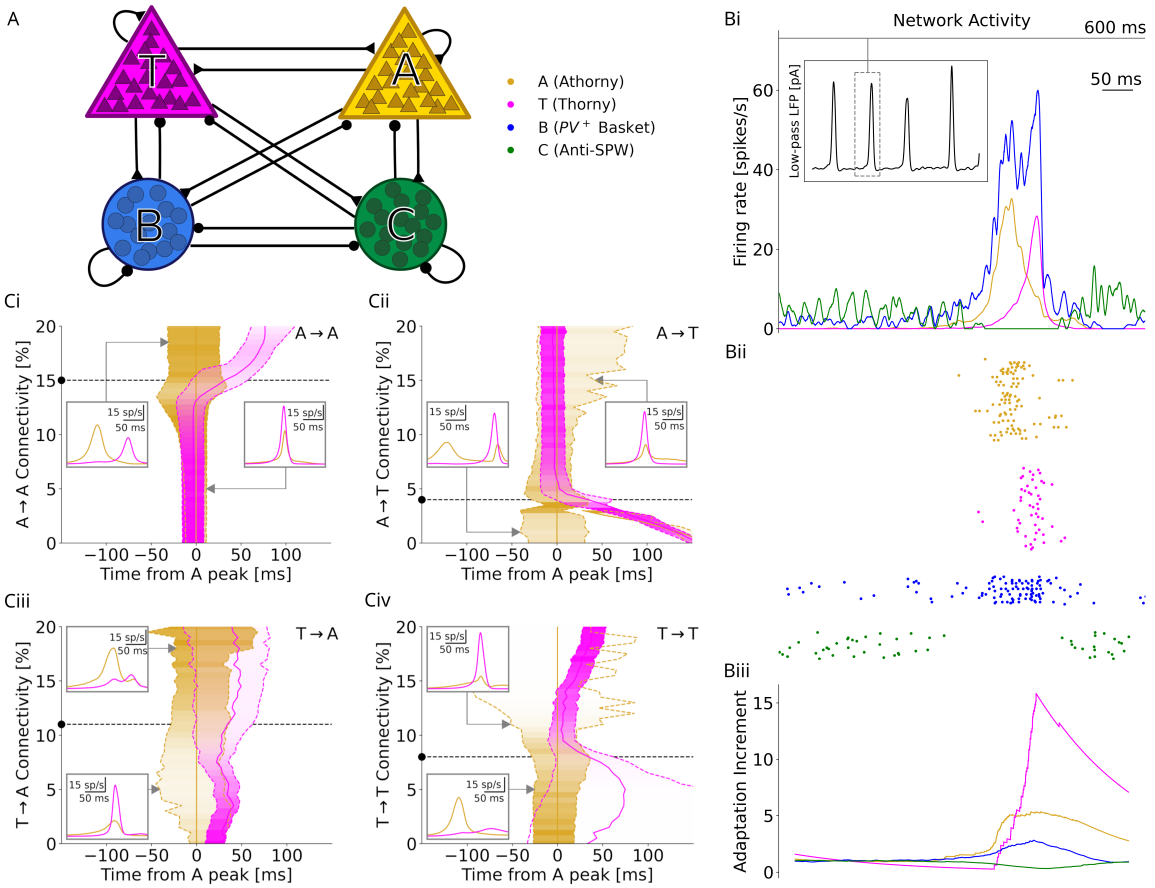

Figure 4: Results of numerical simulations. A, Network scheme. **Bi**, Firing rates before, during, and after a SPW. Inset: low-pass filtered estimate of the LFP over a longer window of 10 s. **ii**, Spike raster plot of a representative sample of each neuron type. **iii**, Relative increment of the average adaptive currents received by each population with respect to a 200 ms baseline before the event. **C**, Effects of varying each connectivity from its default value, marked by a black dashed line and dot. Continuous gold/magenta lines indicate the peak time of each population rate (with the peak of A always plotted at 0), while dashed ones represent the time at which the rate equals 25% of the respective peak. The peak size for each connectivity value is color-coded. Insets: firing trace of each population averaged over many events, for particular connectivity values highlighted by the gray arrows.

peak, with an average 29 ms delay. This delay, which can be observed in both the firing rate and the spike raster plot (Fig. 4Bi-ii), matches the data by Hunt et al. (2018) and can be explained in the following way: immediately after the onset of a SPW, when A neurons are highly active, T neurons are inhibited by the B cells that are excited by the early active A cells. The direct A→T excitation is so little that the main effect of A on T is inhibitory. Only when the firing rate of A cells decreases due to a surge in adaptation (Fig. 4Biii), the activity of T neurons can also grow.

To confirm this intuition and test the robustness of these dynamics, we investigated the effects of varying each of the four excitatory connectivities. We found that the order of firing (A before T) does not depend on connectivity, while the delay between the peaks is strongly affected by it. In particular, for lower values of A→A connectivity, the peaks of A and T are almost simultaneous and the firing times strongly overlap, while they become even more clearly separated when increasing this connectivity (Fig. 4Ci). This happens because the A→A connections amplify the activity of A neurons more strongly and quickly, hence more effectively suppressing T neurons. The A→T connectivity has an opposite effect, with the difference that a second A peak can emerge for particularly low connectivities, because the delay is so long that A cells can partially recover from adaptation (Fig. 4Cii). The role of A→A and A→T connections can thus be understood in relation to each other: if A cells targeted T and A cells in the same proportion (both 15% or both 4% in Fig. 4Ci and Cii), the two populations would be recruited at almost the same time. On the contrary, if direct excitation from A to T neurons were absent, T cells could only fire after most A cells have adapted and fallen silent, with delays even over 100 ms. On the other hand, connections from T neurons have a strong impact on the relative size and amplitude of the peaks of T and A neuron activities, but not much effect on the delay between them (Fig. 4Ciii-iv) because these connections play a role only in the second part of the event. In summary, not only can T cells activate after A cells even if the A→T connectivity is low, but such a low connectivity is also crucial to explain the delay seen in the data by Hunt et al. (2018) and in our model.

In summary, our experimental results show that athorny CA3 pyramidal cells preferentially synapse onto one another, rather than onto their thorny counterparts. This difference is crucial for SPW events to have two distinct peaks and only partially overlapping firing times, as revealed by our spiking model. The model dynamics resemble the data by Hunt et al. (2018) much more closely than the model proposed in the same paper, in which all neurons fire in a few ms and the athorny neurons immediately recruit the thorny cells. The long delay in our model is explained by the ambivalent role of athorny cells, which switch the system to the SPW state, but initially suppress, rather than excite, the thorny pyramids, and later adapt and release the suppression. Our modeling perspective assumes anti-SPW interneurons, which were proposed by Evangelista et al. (2020) to explain the paradoxical triggering of SPWs by *in-vitro* stimulation of PV^+ basket cells (Schlingloff et al., 2014). Although their existence in CA3 has not yet been demonstrated, in CA1 there are NSPW-active interneurons which fall silent during SPWs (Klausberger and Somogyi, 2008),

including a class of CCK^+ basket cells which has also been shown to have a strong reciprocal inhibition with PV^+ baskets (Dudok et al., 2021). However, unlike the model by Evangelista et al. (2020), SPW-NSPW alternations in our model do not depend on synaptic depression on the connections between these interneurons, but on adaptation in pyramidal cells, a mechanism that has been proposed in a different model by Levenstein et al. (2019) and whose efficacy we demonstrated in a spiking network with realistic neural dynamics.

Materials and Methods

Electrophysiology

Ethics approval statement

Animal maintenance and experiments were in accordance with the respective guidelines of local authorities (Berlin state government, T0100/03) and followed the German animal welfare act and the European Council Directive 2010/63/EU on protection of animals used for experimental and other scientific purposes.

Slice preparation

Mice (P25+, average age: P40, both sexes) were decapitated following isoflurane anesthesia. Brains were removed and transferred to ice-cold, sucrose-based artificial cerebrospinal fluid (sACSF) containing (in mM) 50 NaCl, 150 sucrose, 25 $NaHCO_3$, 2.5 KCl, 1 NaH_2PO_4, 0.5 $CaCl_2$, 7.0 $MgCl_2$, 10 glucose, saturated with 95% O_2, 5% CO_2, pH 7.4. Slices (400 μm) were cut in a horizontal plane on a vibratome (VT1200S; Leica) and stored in an interface chamber at 32-34°C. Slices were perfused at a rate of $\sim$1 ml/min with artificial cerebrospinal fluid (ACSF) containing (in mM) 119 NaCl, 26 $NaHCO_3$, 10 glucose, 2.5 KCl, 2.5 $CaCl_2$, 1.3 $MgCl_2$, 1 NaH_2PO_4, and continuously oxygenated with carbogen. Slices were allowed to recover for at least 1.5 hours after preparation before they were transferred into the recording chamber.

Connectivity

Recordings were performed in ACSF at 32–34°C in a submerged-type recording chamber. Cells in the CA3 were identified using infrared differential contrast microscopy (BX51WI, Olympus). We performed somatic whole-cell patch-clamp recordings (pipette resistance 3–5 MΩ) of up to eight cells simultaneously. One cell was stimulated with a train of four action potentials at 20 Hz, elicited by 2–3 ms long current injections of 1.5–4 nA. For characterization to confirm pyramidal cell targeting, increasing steps of current were injected (1 s, increment: 50 pA). In some cells, hyperpolarizing or depolarizing holding current was applied to keep the membrane potential at -60 mV. The intracellular solution contained (in mM) 135 potassium-gluconate,

6.0 KCl, 2.0 $MgCl_2$, 0.2 EGTA, 5.0 Na_2-phosphocreatine, 2.0 Na_2-ATP, 0.5 Na_2-GTP, 10 HEPES buffer, and 0.2% biocytin. The pH was adjusted to 7.2 with KOH. Recordings were performed using Multiclamp 700B amplifiers (Molecular Devices). Signals were filtered at 6 kHz, sampled at 20 kHz and digitized at 16 bit resolution using the Digidata 1550 and pClamp 10.7 (Molecular Devices). A subset of the data ($n = 238$ out of 348 cells) were published in a separate study (Sammons et al., 2024).

Data Analysis — Connectivity

Cells with a membrane potential less negative than -50 mV and a series resistance higher than 30 MΩ were discarded. The connectivity screen underwent a quality control step such that only sweeps were kept if presynaptic action potentials reversed above 0 mV and the membrane potential did not deviate by more then 10 % within a sweep or with reference to the first sweep. Synaptic connections were identified when there was a postsynaptic potential corresponding to the presynaptic stimulation in the averaged trace from 40–50 sweeps. A baseline period (2 ms) just prior to the stimulation and the averaged postsynaptic peak during the first action potential was used for the analysis of the EPSP amplitudes and synaptic delays. Only those pairs in which the first postsynaptic peak was clearly discernible were used for analysis. To analyse short-term plasticity dynamics, postsynaptic traces were deconvolved as described by Richardson and Silberberg (2008). The time constant, τ, was set to 55 ms and the deconvolved trace was low-pass filtered. Subsequent evoked EPSP peaks were then normalised to the first evoked EPSP in the trace. Synaptic dynamics were compared across connection types by comparing the ratio of the first and fourth EPSPs across groups. Failure rate was calculated by dividing the number of sweeps in which an EPSP was observed by the total number of sweeps. This value was calculated for each of the possible four EPSPs corresponding to the four presynaptic action potentials, and then a total sum for each cell was taken. For all boxplots, boxes cover quartiles and whiskers show entire distribution of data excluding outliers, which are shown additionally as filled black circles and considered to be 1.5 x interquartile range. In Fig. 2C,D all data points are shown as coloured, filled circles. Statistics were carried out in Python using the scipy stats module, with a significance level set to 0.05. Data were first checked for normality using the Shapiro-Wilk test. Subsequently, non-parametric tests were performed as appropriate and the Bonferroni correction method was applied to account for multiple comparisons.

Data Analysis — Immunohistochemistry and neuroanatomy of principal cells

After recording, slices were transferred into a fixative solution containing 4% paraformaldehyde in 0.1 M phosphate buffer. Biocytin labelling was revealed by incubating slices in streptavadin conjugated to Alexa 488 (diluted 1:500) overnight in a solution of PBS containing 2.5% normal goat serum and 1% Triton. The slices were then mounted in Mowiol (Sigma-Aldrich). Image stacks of specimens were imaged on an Olympus BX61 FV1000 confocal microscope. Images were taken using a 20X objective with a pixel size of

0.62 μm and a z-step size of 1 μm. The morphology of the pyramidal neurons was scored as 'thorny' or 'athorny' based on the presence or absence of thorny excrescences, respectively. Each cell was scored by at least 3 independent investigators to ensure that in ambiguous cases a consensus was reached. Location of cells relative to the stratum oriens were measured in Fiji (Schindelin et al., 2012) using the line tool and drawing a perpendicular line from the base of the cell soma to the estimated edge of the pyramidal layer at the side of the stratum oriens.

Computational model

Model equations

Neurons are modeled as adaptive exponential (AdEx) integrate-and-fire neurons (Brette and Gerstner, 2005). This level of complexity (two dynamic variables: voltage and adaptation) is necessary to capture the diverse firing patterns of different neural populations. In addition, neuronal adaptation has been proposed as the main mechanism governing the SPW-NSPW alternation (Levenstein et al., 2019). In the AdEx model, the membrane potential V_i of each neuron i evolves according to the equation

$$C\dot{V}_i(t) = -g_L(V_i(t) - E_L) + g_L\Delta_T \exp\left(\frac{V_i(t) - V_T}{\Delta_T}\right) - u_i(t) + I_{ext} + I_{syn}(t) \tag{1}$$

where C is the membrane capacitance, E_L is the resting potential, g_L is the leak conductance, and V_T is the threshold potential. Slightly above this threshold, the membrane potential escapes from the basin of attraction of E_L and begins an exponential upswing with a slope Δ_T. As soon as the upswing reaches a conventional value V_{stop}, a spike is emitted and V_i is reset to a value V_{reset} and fixed there for a refractory time τ_{ref}. Neurons receive an internal feedback inhibition $u_i(t)$, representing an adaptive current, which evolves according to

$$\tau_u \dot{u}_i(t) = -u_i(t) + a(V_i(t) - E_L) \tag{2}$$

in which a is the voltage-coupling of adaptation and τ_u is its timescale. Upon spiking, u is increased by an amount b (spike-triggered adaptation). Neurons receive a constant external input I_{ext} and a synaptic current $I_{syn}(t) = \sum_J g_i^J(t)(V_i(t) - E_{rev}^J)$, where E_{rev}^J is the reversal potential for the neurotransmitter used by the pre-synaptic population J, and $g_i^J(t)$ is the total synaptic conductance received from the neurons in population J, which obeys

$$\dot{g}_i^J(t) = -\frac{g_i^J}{\tau_d^J} + \sum_{f,j} \delta(t - t_j^f - \tau_l) p_{IJ} w_{IJ}, \tag{3}$$

where τ_d^J is the synaptic decay constant for population J, and τ_l is the synaptic latency. The contribution of each pre-synaptic spike at time t_j^f is determined by a connection probability $p_{IJ} \in [0, 1]$ and a weight

w_{IJ}.

Single neuron parameters

We consider four different neural populations: thorny pyramids (T), athorny pyramids (A), PV$^+$-basket cells (B), and anti-SPW interneurons (C). The latter are modeled as CCK$^+$-basket cells. For each population, parameters were chosen in order to be close to the single-neuron physiology. For A and T neurons, we follow the main figures and supplementary data by Hunt et al. (2018) and Linaro et al. (2022), since they performed detailed single-neuron physiological characterization of the two neuron types. Namely, athorny neurons were shown to have a higher input resistance, a higher resting potential, and a lower firing threshold than their thorny counterparts, and both kinds have a high reset potential. In particular, we reset athorny neurons above the threshold, because this is how the AdEx model produces bursting (Naud et al., 2008), a feature that has been reported in this cell type (Hunt et al., 2018). Our parameters result in a lower rheobase for athorny than for thorny neurons (Hunt et al. (2018), Linaro et al. (2022), Fig. S1). Interneuron parameters were based on data from CA3, if available (Fidzinski et al., 2015; Pelkey et al., 2017), or otherwise from other hippocampal subfields (Ledri et al., 2012; Pawelzik et al., 2002; Tricoire et al., 2011).

The parameters of adaptation cannot be directly compared to physiological values, because this variable summarizes a multitude of different currents, each with its own size and timescale (Benda, 2021). Therefore, we firstly aimed at reproducing the f-I curves of different neurons, when available (Fig. S2). Thorny and athorny f-I curves were compared to those measured by Linaro et al. (2022), while for PV$^+$-basket cells we used CA3 data from Fidzinski et al. (2015). In addition, the large spike-coupling b and long timescale τ_u of pyramidal adaptation allow to reproduce the strong firing rate accommodation typical of these cells (Storm, 1990; Hunt et al., 2018), while these parameters are smaller in A and especially B cells, which can sustain a high firing rate without significant accommodation (Pelkey et al., 2017). In the AdEx model, if the voltage-coupling a is strong enough, spiking happens through a Hopf bifurcation, which is responsible for phenomena like transient spiking and class 2 behaviour (Touboul and Brette, 2008). Therefore we set this parameter to 0 for thorny cells, in which these behaviours are absent, and to a higher value for athorny cells, which seem to exhibit transient spiking for intermediate values of a constant input (Hunt et al., 2018), and for interneurons. In particular, for B cells, we could reproduce the discontinuity around 15 Hz typical of fast-spiking interneurons (Gerstner et al., 2014). Neuronal parameters and their values are summarized in Table 1.

Network parameters

Each population size is based on an estimation of its representation in a 400-μm-thick CA3 slice, according to the quantitative assessment by Bezaire and Soltesz (2013). Pyramidal neurons are divided into thorny

		Athorny (A)	Thorny (T)	PV$^+$-Basket (B)	Anti-SPW (C)
Population size		2700	5300	150	100
C	[pF]	200	200	100	100
g_L	[nS]	8	11	8	5
E_L	[mV]	-60	-70	-55	-57
V_{thr}	[mV]	-48	-44	-40	-40
V_{reset}	[mV]	-42	-46	-57	-52
a	[nS]	4	0	6	2.5
b	[pA]	85	150	25	20
τ_u	[ms]	200	200	50	100
τ_{ref}	[ms]	3	3	3	3
Δ_T	[mV]	2.5	2.5	2.5	2.5
I_{ext}	[pA]	140	285	180	160

Table 1: Single neuron parameters

and athorny according to the 66%-34% ratio that we determined experimentally. The background currents I_{ext} are constant and correspond to the non-transient rheobase ρ, plus 10%, with the exception of population A, which receives +40% because it is responsible for keeping the other neurons inhibited for most of the time. This assumption is reasonable, since CCK$^+$-basket cells "receive a far less efficient local excitatory drive, but are exposed to modulatory effects of extrinsic inputs" (Freund, 2003).

Neurons are connected to each other with a probability p_{IJ}, depending on the pre- and post-synaptic population J and I. For excitatory-to-excitatory connections, these probabilities have the values that we assessed experimentally. For the other connections, the existent literature is too inconsistent to derive coherent conclusions (Gulyás et al., 1993; Maccaferri et al., 2000; Mátyás et al., 2004; Bezaire and Soltesz, 2013; Campanac et al., 2013; Kohus et al., 2016; Pelkey et al., 2017; Dudok et al., 2021): therefore, in order to minimize the number of assumptions not based on solid evidence, they were all given the same probability 0.2.

Excitatory-to-excitatory synaptic weights were all set to 0.2 nS, since differences in EPSP sizes were not found to be significant (Figure 2C). This values corresponds to an EPSP size of 0.1 mV, which is lower than the ones measured experimentally, but compensates for the fact that they directly affect the (somatic) membrane potential of the post-synaptic neurons neurons and that connections are homogeneous. The other weights were chosen in order to satisfy the basic requirements for bistability and disinhibition dynamics, other than to produce realistic incidence and duration of SPWs and firing rates of the different populations. The search for the bistable region of the parameter space was guided by the insights previously obtained in the bifurcation analysis of a three-population model of CA3 (Evangelista et al., 2020). Although our model has one more population, we found that the basic requirements are the same: pyramidal cells need to more strongly excite interneurons B and to be more strongly inhibited by interneurons C. In addition, populations C and B need to have strong inhibitory couplings between each other. For firing rate requirements, we assumed, following Evangelista et al. (2020), that C neurons fire $\sim$10 spikes/s in NSPW

states and are almost silent during SPWs. For B neurons, we based on estimates of 5-10 spikes/s in the NSPW periods and fast spiking at 50–70 during SPWs (Klausberger and Somogyi, 2008; Lapray et al., 2012; Varga et al., 2012; Hájos et al., 2013). Pyramidal neurons are almost silent (0–1 spikes/s) in NSPW periods and fire on average 10–20 spikes/s in SPW events (Klausberger and Somogyi, 2008; Lapray et al., 2012; Hájos et al., 2013; English et al., 2014). In order to satisfy these requirements, excitatory weights needed to be about one order of magnitude smaller than inhibitory ones, which is partially in accordance with the hippocampal interneuron literature mentioned above, and partially necessary because not all kinds of interneurons are included in the network.

Regarding the other synaptic parameters, all the latencies were set to 1 ms, glutamatergic and GABAergic reversal potentials have the typical values of 0 mV and -70 mV respectively, and the former are assumed to be twice as fast as the latter (Geiger et al., 1995; Bartos et al., 2002). Network parameters are summarized in Table 2.

		From A	From T	From B	From C
p_{AI}		15%	11%	20%	20%
p_{TI}		4%	8%	20%	20%
p_{BI}		20%	20%	20%	20%
p_{CI}		20%	20%	20%	20%
w_{AI}	[nS]	0.2	0.2	2.15	15
w_{TI}	[nS]	0.2	0.2	0.8	15
w_{BI}	[nS]	0.7	0.5	6	9
w_{CI}	[nS]	0.1	0.05	5	3
τ_d	[ms]	2	2	4	4
E_{rev}	[mV]	0	0	-70	-70
τ_l	[ms]	1	1	1	1

Table 2: Network parameters

Network activity

SPW events are identified based on the current flowing from B cells to the excitatory ones, which is thought to represent most of the LFP signal observed in the *stratum pyramidale*. This signal is low-pass filtered up to 5 Hz, in order to cover the whole duration of an event. In this signal, peaks higher than 50 pA are regarded as SPWs. The beginning and end of the events are defined as the times at which the low-pass-filtered LFP crosses the value $\frac{1}{2}(L_p - L_0)$, where L_p is the LFP peak of each event and L_0 is a baseline value.

Acknowledgements

The authors would like to thank Susanne Rieckmann and Anke Schönherr for excellent technical assistance, Linda Brenndörfer for help with confocal microscopy and Antje Fortströer for administrative assis-

tance. Funding sources: German Research Foundation: project 327654276 – SFB 1315 (DS, RK), project 184695641 – SFB 958 (DS), project 415914819 – FOR 3004 (DS), project 431572356 (DS); Germany's Excellence Strategy – Exc-2049-390688087 (NeuroCure to DS, RPS and MO), project 503954250 (MO); European Research Council Horizon 2020 grant 810580 – BrainPlay (DS); Federal Ministry of Education and Research project 01GQ1420B – SmartAge (DS).

Author Contributions

Conceptualisation: RPS, GC, NM, SM, RK, DS. **Methodology**: RPS, SM, AS, MO, NM. **Software**: SM, GC. **Validation**: RPS, SM, LMV, VDM, GC, AS, MO, NM, RK, DS. **Formal Analysis**: RPS, SM. **Investigation**: RPS, LMV, VDM, NM. **Resources**: RK, DS. **Data Curation**: RPS, SM, AS, MO. **Writing - Original draft**: RPS, SM. **Writing - Review and editing**: RPS, SM, LMV, VDM, GC, AS, MO, NM, RK, DS. **Visualisation**: RPS, SM. **Supervision**: RPS, RK, DS. **Project Administration**: RPS, SM, RK, DS. **Funding Acquisition**: RPS, MO, RK, DS.

References

Bartos, M., Vida, I., Frotscher, M., Meyer, A., Monyer, H., Geiger, J. R., and Jonas, P. (2002). Fast synaptic inhibition promotes synchronized gamma oscillations in hippocampal interneuron networks. *Proceedings of the National Academy of Sciences*, 99(20):13222–13227.

Benda, J. (2021). Neural adaptation. *Current Biology*, 31(3):R110–R116.

Bezaire, M. J. and Soltesz, I. (2013). Quantitative assessment of ca1 local circuits: knowledge base for interneuron-pyramidal cell connectivity. *Hippocampus*, 23(9):751–785.

Bilkey, D. K. and Schwartzkroin, P. A. (1990). Variation in electrophysiology and morphology of hippocampal CA3 pyramidal cells. *Brain Research*, 514(1):77–83.

Brette, R. and Gerstner, W. (2005). Adaptive exponential integrate-and-fire model as an effective description of neuronal activity. *Journal of neurophysiology*, 94(5):3637–3642.

Campanac, E., Gasselin, C., Baude, A., Rama, S., Ankri, N., and Debanne, D. (2013). Enhanced intrinsic excitability in basket cells maintains excitatory-inhibitory balance in hippocampal circuits. *Neuron*, 77(4):712–722.

Cembrowski, M. S. and Spruston, N. (2019). Heterogeneity within classical cell types is the rule: lessons from hippocampal pyramidal neurons. *Nature Reviews Neuroscience*, 20(4):193–204.

339 Dudok, B., Klein, P. M., Hwaun, E., Lee, B. R., Yao, Z., Fong, O., Bowler, J. C., Terada, S., Sparks,
340 F. T., Szabo, G. G., et al. (2021). Alternating sources of perisomatic inhibition during behavior. *Neuron*,
341 109(6):997–1012.

342 English, D. F., Peyrache, A., Stark, E., Roux, L., Vallentin, D., Long, M. A., and Buzsáki, G. (2014).
343 Excitation and inhibition compete to control spiking during hippocampal ripples: intracellular study in
344 behaving mice. *Journal of Neuroscience*, 34(49):16509–16517.

345 Evangelista, R., Cano, G., Cooper, C., Schmitz, D., Maier, N., and Kempter, R. (2020). Generation of
346 sharp wave-ripple events by disinhibition. *Journal of Neuroscience*, 40(41):7811–7836.

347 Fidzinski, P., Korotkova, T., Heidenreich, M., Maier, N., Schuetze, S., Kobler, O., Zuschratter, W.,
348 Schmitz, D., Ponomarenko, A., and Jentsch, T. J. (2015). Kcnq5 k+ channels control hippocampal
349 synaptic inhibition and fast network oscillations. *Nature communications*, 6(1):6254.

350 Fitch, J. M., Juraska, J. M., and Washington, L. W. (1989). The dendritic morphology of pyramidal
351 neurons in the rat hippocampal CA3 area. I. Cell types. *Brain Research*, 479(1):105–114.

352 Freund, T. F. (2003). Interneuron diversity series: rhythm and mood in perisomatic inhibition. *Trends in*
353 *neurosciences*, 26(9):489–495.

354 Geiger, J. R., Melcher, T., Koh, D.-S., Sakmann, B., Seeburg, P. H., Jonas, P., and Monyer, H. (1995).
355 Relative abundance of subunit mrnas determines gating and ca2+ permeability of ampa receptors in
356 principal neurons and interneurons in rat cns. *Neuron*, 15(1):193–204.

357 Gerstner, W., Kistler, W. M., Naud, R., and Paninski, L. (2014). *Neuronal dynamics: From single neurons*
358 *to networks and models of cognition*. Cambridge University Press.

359 Gulyás, A. I., Miles, R., Hájos, N., and Freund, T. F. (1993). Precision and variability in postsynaptic
360 target selection of inhibitory cells in the hippocampal CA3 region. *The European Journal of Neuroscience*,
361 5(12):1729–1751.

362 Hájos, N., Karlócai, M. R., Németh, B., Ulbert, I., Monyer, H., Szabó, G., Erdélyi, F., Freund, T. F., and
363 Gulyás, A. I. (2013). Input-output features of anatomically identified ca3 neurons during hippocampal
364 sharp wave/ripple oscillation in vitro. *Journal of Neuroscience*, 33(28):11677–11691.

365 Hunt, D. L., Linaro, D., Si, B., Romani, S., and Spruston, N. (2018). A novel pyramidal cell type promotes
366 sharp-wave synchronization in the hippocampus. *Nature Neuroscience*, 21(7):985–995.

367 Klausberger, T. and Somogyi, P. (2008). Neuronal diversity and temporal dynamics: the unity of hip-
368 pocampal circuit operations. *Science*, 321(5885):53–57.

Kohus, Z., Káli, S., Rovira-Esteban, L., Schlingloff, D., Papp, O., Freund, T., Hájos, N., and Gulyás, A. (2016). Properties and dynamics of inhibitory synaptic communication within the CA3 microcircuits of pyramidal cells and interneurons expressing parvalbumin or cholecystokinin. *The Journal of physiology*, 594(13):3745–3774.

Lapray, D., Lasztoczi, B., Lagler, M., Viney, T. J., Katona, L., Valenti, O., Hartwich, K., Borhegyi, Z., Somogyi, P., and Klausberger, T. (2012). Behavior-dependent specialization of identified hippocampal interneurons. *Nature neuroscience*, 15(9):1265–1271.

Ledri, M., Nikitidou, L., Erdelyi, F., Szabo, G., Kirik, D., Deisseroth, K., and Kokaia, M. (2012). Altered profile of basket cell afferent synapses in hyper-excitable dentate gyrus revealed by optogenetic and two-pathway stimulations. *European Journal of Neuroscience*, 36(1):1971–1983.

Lee, H., Wang, C., Deshmukh, S. S., and Knierim, J. J. (2015). Neural Population Evidence of Functional Heterogeneity along the CA3 Transverse Axis: Pattern Completion versus Pattern Separation. *Neuron*, 87(5):1093–1105.

Levenstein, D., Buzsáki, G., and Rinzel, J. (2019). Nrem sleep in the rodent neocortex and hippocampus reflects excitable dynamics. *Nature communications*, 10(1):1–12.

Linaro, D., Levy, M. J., and Hunt, D. L. (2022). Cell type-specific mechanisms of information transfer in data-driven biophysical models of hippocampal ca3 principal neurons. *PLoS Computational Biology*, 18(4):e1010071.

Maccaferri, G., David, J., Roberts, B., Szucs, P., Cottingham, C. A., and Somogyi, P. (2000). Cell surface domain specific postsynaptic currents evoked by identified gabaergic neurones in rat hippocampus in vitro. *The Journal of physiology*, 524(1):91–116.

Marissal, T., Bonifazi, P., Picardo, M. A., Nardou, R., Petit, L. F., Baude, A., Fishell, G. J., Ben-Ari, Y., and Cossart, R. (2012). Pioneer glutamatergic cells develop into a morpho-functionally distinct population in the juvenile CA3 hippocampus. *Nature Communications*, 3:1316.

Mátyás, F., Freund, T. F., and Gulyás, A. I. (2004). Convergence of excitatory and inhibitory inputs onto cck-containing basket cells in the ca1 area of the rat hippocampus. *European Journal of Neuroscience*, 19(5):1243–1256.

Naud, R., Marcille, N., Clopath, C., and Gerstner, W. (2008). Firing patterns in the adaptive exponential integrate-and-fire model. *Biological cybernetics*, 99:335–347.

Pawelzik, H., Hughes, D. I., and Thomson, A. M. (2002). Physiological and morphological diversity of immunocytochemically defined parvalbumin-and cholecystokinin-positive interneurones in ca1 of the adult rat hippocampus. *Journal of Comparative Neurology*, 443(4):346–367.

Pelkey, K. A., Chittajallu, R., Craig, M. T., Tricoire, L., Wester, J. C., and McBain, C. J. (2017). Hippocampal gabaergic inhibitory interneurons. *Physiological reviews*, 97(4):1619–1747.

Richardson, M. J. E. and Silberberg, G. (2008). Measurement and Analysis of Postsynaptic Potentials Using a Novel Voltage-Deconvolution Method. *Journal of Neurophysiology*, 99(2):1020–1031.

Sammons, R. P., Vezir, M., Moreno-Velasquez, L., Cano, G., Orlando, M., Sievers, M., Grasso, E., Metodieva, V. D., Kempter, R., Schmidt, H., and Schmitz, D. (2024). Structure and function of the hippocampal CA3 module. *Proceedings of the National Academy of Sciences of the United States of America*, 121(6):e2312281120.

Schindelin, J., Arganda-Carreras, I., Frise, E., Kaynig, V., Longair, M., Pietzsch, T., Preibisch, S., Rueden, C., Saalfeld, S., Schmid, B., Tinevez, J.-Y., White, D. J., Hartenstein, V., Eliceiri, K., Tomancak, P., and Cardona, A. (2012). Fiji: an open-source platform for biological-image analysis. *Nature Methods*, 9(7):676–682. Publisher: Nature Publishing Group.

Schlingloff, D., Káli, S., Freund, T. F., Hájos, N., and Gulyás, A. I. (2014). Mechanisms of sharp wave initiation and ripple generation. *Journal of Neuroscience*, 34(34):11385–11398.

Soltesz, I. and Losonczy, A. (2018). CA1 pyramidal cell diversity enabling parallel information processing in the hippocampus. *Nature Neuroscience*, 21(4):484–493.

Storm, J. F. (1990). Potassium currents in hippocampal pyramidal cells. *Progress in brain research*, 83:161–187.

Sun, Q., Sotayo, A., Cazzulino, A. S., Snyder, A. M., Denny, C. A., and Siegelbaum, S. A. (2017). Proximodistal Heterogeneity of Hippocampal CA3 Pyramidal Neuron Intrinsic Properties, Connectivity, and Reactivation during Memory Recall. *Neuron*, 95(3):656–672.e3.

Touboul, J. and Brette, R. (2008). Dynamics and bifurcations of the adaptive exponential integrate-and-fire model. *Biological cybernetics*, 99(4-5):319.

Tricoire, L., Pelkey, K. A., Erkkila, B. E., Jeffries, B. W., Yuan, X., and McBain, C. J. (2011). A blueprint for the spatiotemporal origins of mouse hippocampal interneuron diversity. *Journal of Neuroscience*, 31(30):10948–10970.

Valero, M. and de la Prida, L. M. (2018). The hippocampus in depth: a sublayer-specific perspective of entorhinal-hippocampal function. *Current Opinion in Neurobiology*, 52:107–114.

Varga, C., Golshani, P., and Soltesz, I. (2012). Frequency-invariant temporal ordering of interneuronal discharges during hippocampal oscillations in awake mice. *Proceedings of the National Academy of Sciences*, 109(40):E2726–E2734.

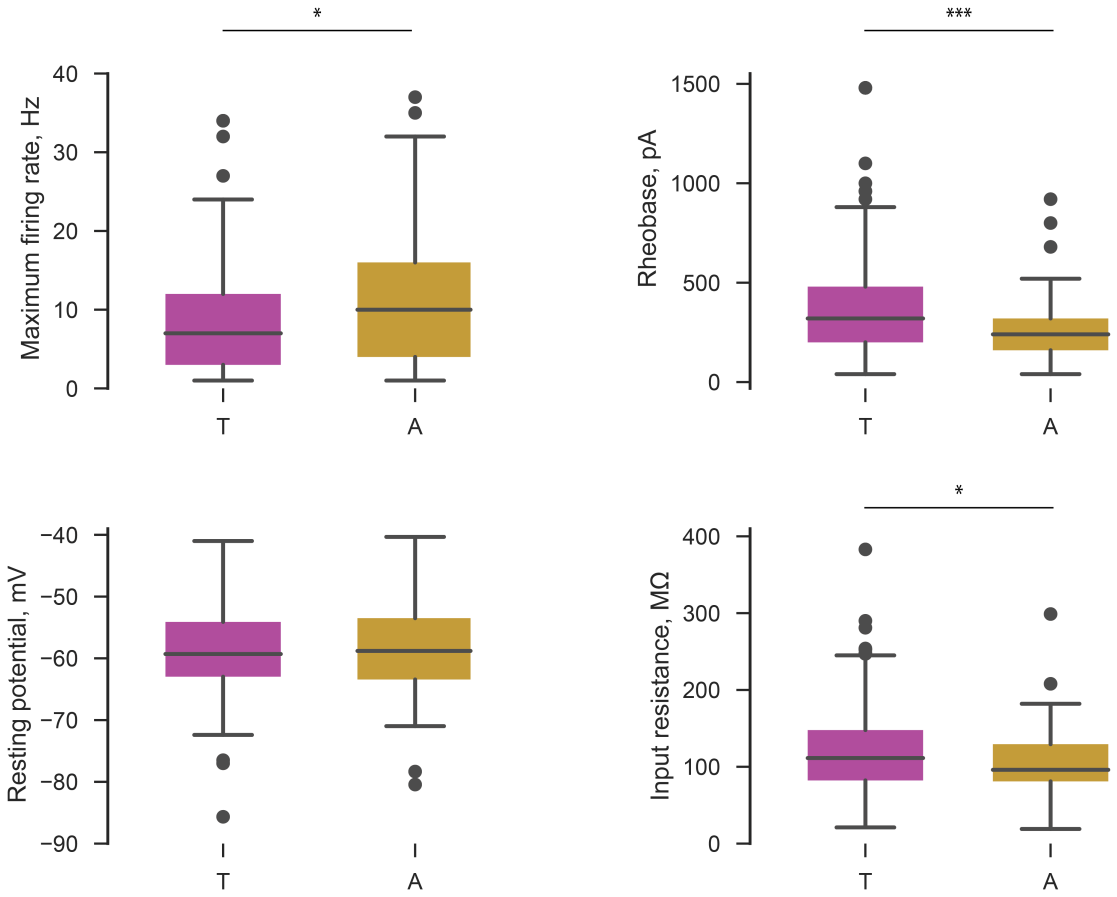

Figure S1: Intrinsic properties of thorny (T) and athorny (A) cells. Significance calculated using Mann-Whitney-U and corrected for multiple comparisons. *** $p < 0.001$, * $p < 0.05$.

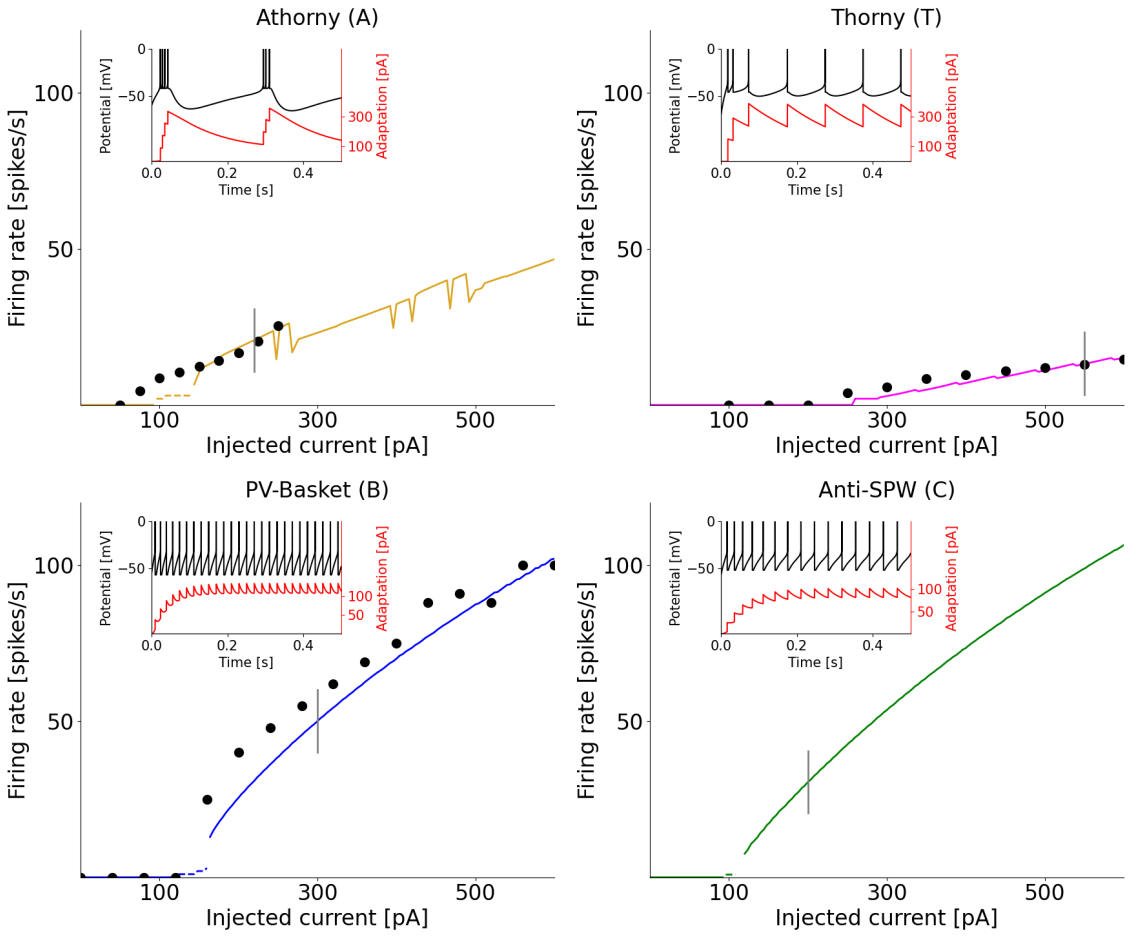

Figure S2: Onset f-I curves for each neuron type, calculated, for comparability, by delivering a constant current for 500 ms, like in Hunt et al. (2018). These curves (colored solid lines) are compared to experimental data (black dots) from Hunt et al. (2018) for A and T neurons, and from Fidzinski et al. (2015) for B neurons. Dashed lines represent transient firing. Insets: example of firing patterns displayed by the different neurons in response to the specific current values marked by vertical gray lines in the main figure.